



Correlated Hofstadter spectrum and flavour phase diagram in magic-angle twisted bilayer graphene

Jiachen Yu^{1,2}, Benjamin A. Foutty^{2,3}, Zhaoyu Han[®]³, Mark E. Barber[®]^{1,2}, Yoni Schattner^{3,4}, Kenji Watanabe[®]⁵, Takashi Taniguchi[®]⁶, Philip Phillips[®]⁷, Zhi-Xun Shen[®]^{1,2,3,4}, Steven A. Kivelson^{2,3} and Benjamin E. Feldman[®]^{2,3,4} ≅

In magic-angle twisted bilayer graphene, the moiré superlattice potential gives rise to narrow electronic bands that support a multitude of many-body quantum phases. Further richness arises in the presence of a perpendicular magnetic field, where the interplay between moiré and magnetic length scales leads to fractal Hofstadter subbands. In this strongly correlated Hofstadter platform, multiple experiments have identified gapped topological and correlated states, but little is known about the phase transitions between them in the intervening compressible regimes. Here we simultaneously unveil sequences of broken-symmetry Chern insulators and resolve sharp phase transitions between competing states with different topological quantum numbers and different occupations of the spin-valley flavour. Our measurements determine the energy spectrum of interacting Hofstadter subbands in magic-angle twisted bilayer graphene and map out the phase diagram of flavour occupancy. In addition, we observe full lifting of the degeneracy of the zeroth Landau levels together with level crossings, indicating moiré valley splitting. We propose a unified flavour polarization mechanism to understand the intricate interplay of topology, interactions and symmetry breaking as a function of density and applied magnetic field in this system.

hen two monolayer graphene sheets are twisted near a magic angle of 1.1° , spatially modulated interlayer tunnelling generates a pair of flat electronic bands at low energies¹. The combination of quenched kinetic energies and multiple quantum degrees of freedom renders the system prone to various intriguing correlation-driven phases characterized by spontaneously broken symmetry²⁻³³. At zero magnetic field, a cascade of Stoner-type transitions was reported^{9,10} to result in a series of changes in flavour polarization and a sawtooth pattern of inverse compressibility as a function of the number of electrons per moiré unit cell, ν . The same mechanism underlies the recent observation^{11,12} of a Pomeranchuk effect at $\nu = \pm 1$.

In a perpendicular magnetic field B, moiré systems develop a fractal energy spectrum in the noninteracting limit known as the Hofstadter butterfly³⁴ that depends on the number of flux quanta Φ/Φ_0 per moiré unit cell. Although the Hofstadter spectrum for magic-angle twisted bilayer graphene (MATBG) has only been theoretically calculated at a single-particle level^{35–39}, its flat electronic bands open up new opportunities to investigate Hofstadter-butterfly physics in the strongly correlated regime. Recent studies have identified a series of robust correlated Chern insulators (ChIs) at moderate fields, which have been interpreted in terms of flavour-polarized states in which only subsets of the underlying Chern bands 15,17,18 or Hofstadter subbands^{13,14,16} are occupied, with a driving mechanism analogous to quantum Hall ferromagnetism. Most studies have focused only on the flavour polarization/degeneracy of the ChIs themselves, with limited insight between the incompressible states. Moreover, the many-body Hofstadter spectrum has not been measured in MATBG or any other solid-state system, and it remains poorly understood theoretically.

Here we measure the local inverse electronic compressibility $d\mu$ dn (μ , chemical potential; n, density) of MATBG using a scanning single-electron transistor (SET). Our measurements reveal unexpected sequences of broken-symmetry ChIs at high fields, demonstrate how they evolve from the sawtooth pattern of electronic compressibility at low fields and enable us to quantitatively extract the strongly correlated Hofstadter spectrum. We further observe multiple sharp features that exhibit negative $d\mu/dn$, which correspond to flavour phase transitions, some of which are first order and exhibit hysteresis. Because our thermodynamic probe is sensitive in both compressible and incompressible regimes, we are able to pinpoint exactly where phase transitions occur and construct a phase diagram of the number of partially occupied (or 'active') flavours as a function of ν and B. Finally, we observe broken-symmetry quantum Hall states emanating from the charge neutrality point (CNP) at all integer Landau level (LL) fillings $\nu_C = n\Phi_0/B$ and apparent LL crossings at $\nu_c = \pm 2$ (the subscript refers to the Chern number C). These behaviours suggest that mirror symmetry (M_{ν}) breaking causes an energetic splitting of the moiré valleys that occur at inequivalent corners of the hexagonal moiré Brillouin zone (mBZ) for each graphene valley. The nanoscale resolution of the SET renders it less susceptible to spatial inhomogeneity and allows us to disentangle which of these phenomena are robust and which are sensitive to local details such as twist angle.

Correlated broken-symmetry Hofstadter butterfly

An optical micrograph of the sample and schematic of the experimental setup are respectively shown in Fig. 1a and 1b (Methods and Supplementary Section 1). At B=0, $d\mu/dn$ exhibits a sawtooth-like pattern (Fig. 1c), and measurements as a function of position

¹Department of Applied Physics, Stanford University, Stanford, CA, USA. ²Geballe Laboratory of Advanced Materials, Stanford University, Stanford, CA, USA. ³Department of Physics, Stanford University, Stanford, CA, USA. ⁴Stanford Institute for Materials and Energy Sciences, SLAC National Accelerator Laboratory, Menlo Park, CA, USA. ⁵Research Center for Functional Materials, National Institute for Material Science, Tsukuba, Japan. ⁶International Center for Materials Nanoarchitectonics, National Institute for Material Science, Tsukuba, Japan. ⁷Department of Physics and Institute for Condensed Matter Theory, University of Illinois at Urbana-Champaign, Urbana, IL, USA. [⊠]e-mail: bef@stanford.edu

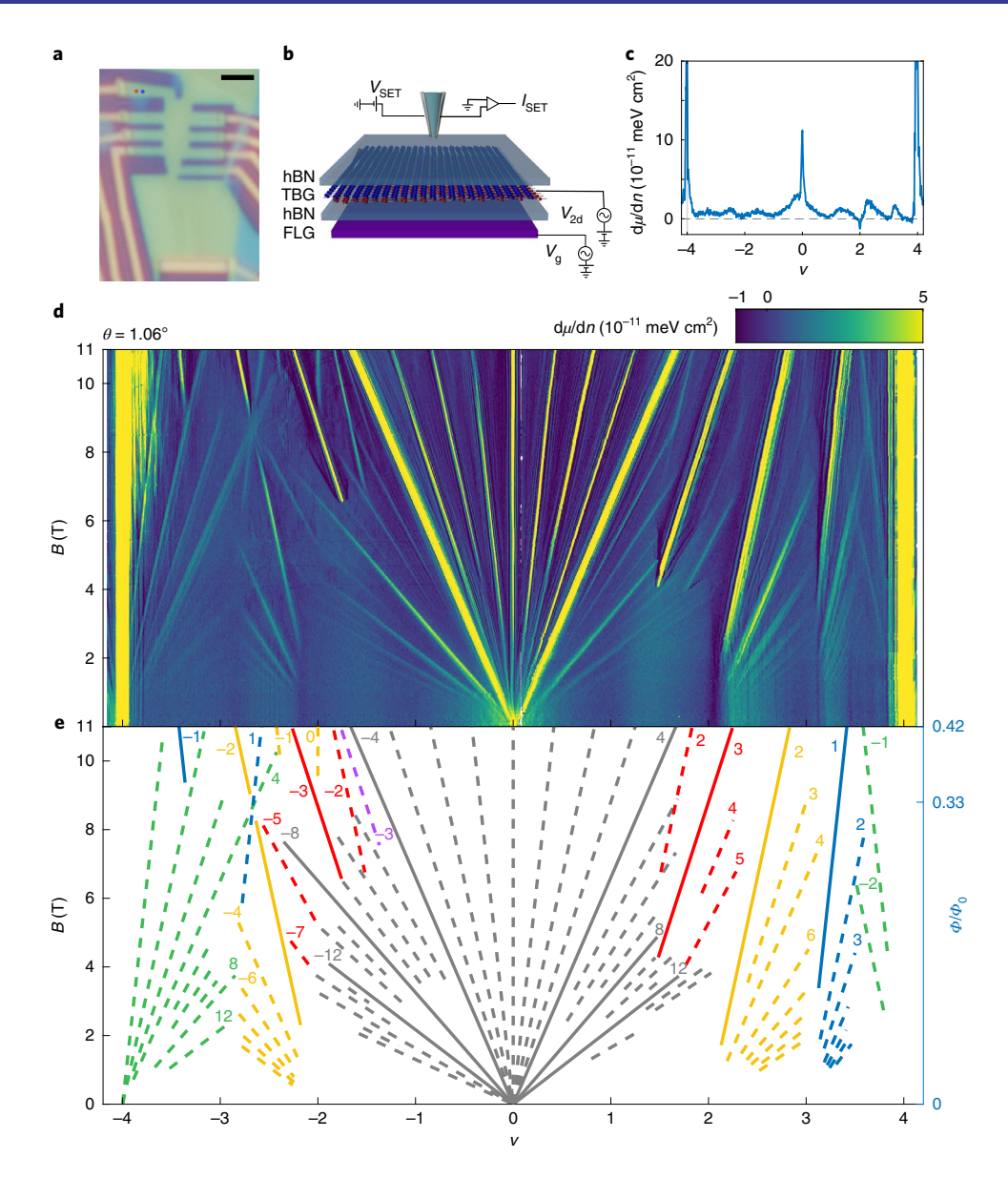


Fig. 1 Device geometry and local electronic compressibility of MATBG. **a**, Optical micrograph of the MATBG device. Scale bar, 2 μm. **b**, Schematic of the measurement setup (Methods). TBG, twisted bilayer graphene; V_{SET} , voltage bias applied to the SET probe; I_{SET} , measured current through the SET. **c**, Inverse electronic compressibility $d\mu/dn$ measured as a function of the moiré filling factor ν at a perpendicular magnetic field of B = 0. **d**, $d\mu/dn$ as a function of ν and B, measured at the location marked by the red dot in **a** with twist angle $\theta = 1.06^{\circ}$. Data are truncated at $-1 \times 10^{-11} \sim 5 \times 10^{-11} \text{meV cm}^2$ in the colour map. **e**, Incompressible (gapped) states identified from **d**. Selected states are labelled by their slope t. Grey, red, yellow, blue, green and purple correspond to states with different integer and fractional intercepts (-1/2), respectively. Solid lines represent the strongest state in each group. For the zLLs, they denote multiples of |t| = 4.

demonstrate similar behaviour over a range of twist angles at different locations (Extended Data Fig. 1). All integer fillings including the CNP are gapless, indicating that the hexagonal boron nitride (hBN) is not aligned. The findings presented below differ from and complement a recent local compressibility study of an aligned device²⁰. In this paper, we focus on the behaviour of MATBG in a perpendicular field, where we observe multiple interpenetrating incompressible states (Fig. 1d). Each satisfies the Diophantine equation⁴⁰, $\nu = t(\Phi/\Phi_0) + s$, where t is the sum of the Chern numbers of all filled bands and s is the band filling index. Figure 1e shows the experimentally determined Wannier diagram⁴⁰.

The incompressible states can be grouped into sequences based on their intercepts at B=0. When s=0, they correspond to LLs originating from the CNP (herein, we refer to all s=0 LLs as zeroth LLs (zLLs) and label them by $\nu_C \equiv t$). We observe all the integer

zLL states with $|\nu_C|$ < 4, which implies full symmetry breaking. This includes lifting of the degeneracy that would arise from the presence of two degenerate moiré valleys, which we discuss in more detail at the end of the manuscript. We also observe a series of LLs emanating from the moiré superlattice band gaps at |s| = 4 that point towards lower density (Fig. 1d). They are much weaker than the zLLs, indicating that the narrow bands are less dispersive close to the superlattice gaps compared with near the CNP. Finally, gapped states with 0 < |s| < 4 are ChIs. The low-field ChI sequences are consistent with earlier reports^{3–5,13,18,41}, as are the strongest ChIs, which satisfy the relation |s| + |t| = 4 at high fields^{13–19}. These ChIs appear over a range of twist angles (Extended Data Fig. 2). They are independently confirmed by the changes in local conductivity probed by scanning microwave impedance microscopy (MIM) (Extended Data Fig. 3).

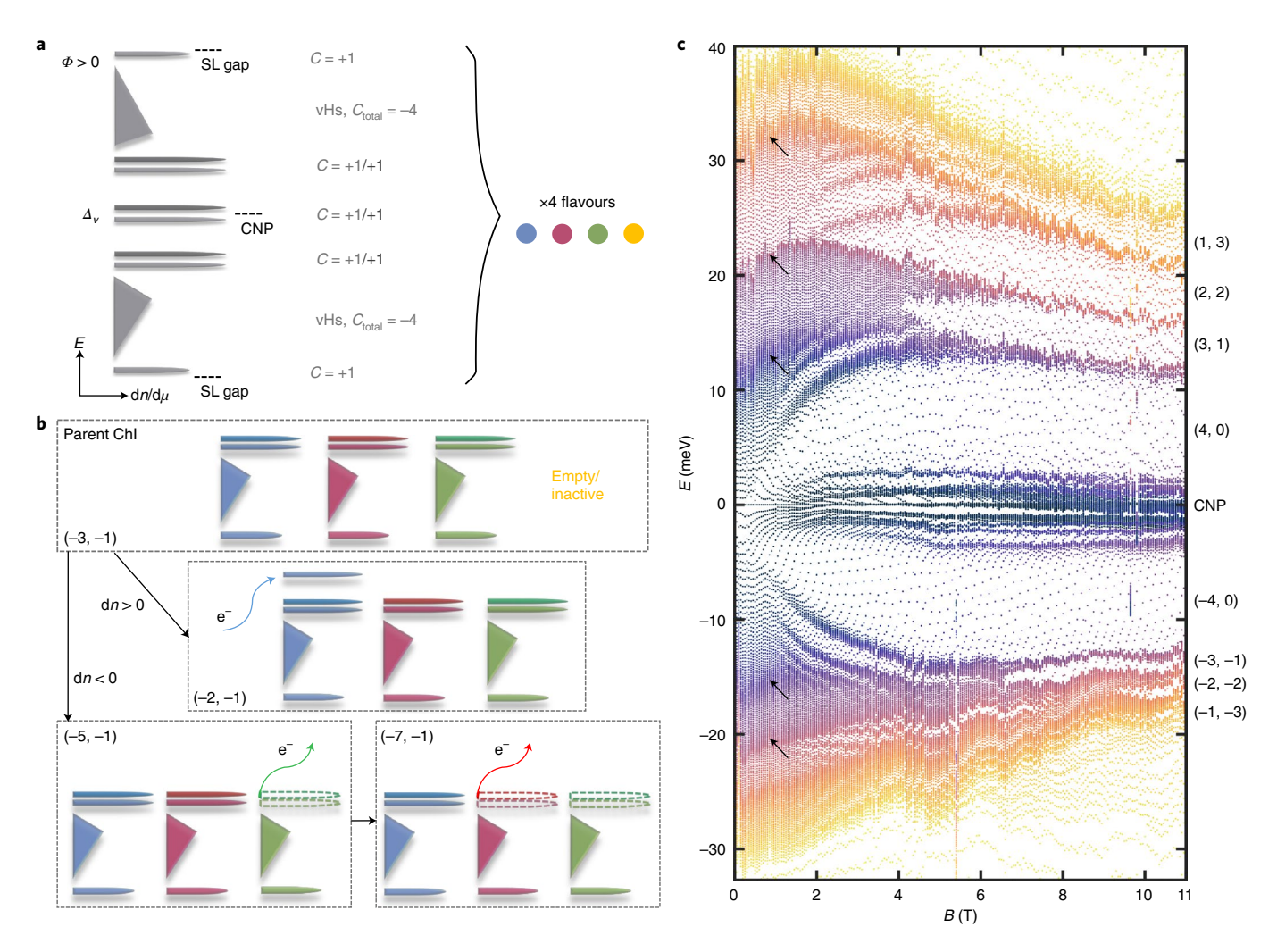


Fig. 2 | Flavour polarization and correlated Hofstadter spectrum. a, Schematic of Hofstadter subbands (grey) for a single flavour at fixed flux per moiré unit cell $\Phi > 0$. The Chern number (C) of each subband is labelled on the right. vHs denotes subbands close to the van Hove singularity that are unresolved due to broadening/disorder. The C = +1/+1 doublets near the CNP reflect the possibility of moiré valley splitting, Δ_v , b, Illustration of flavour occupancy of the broken-symmetry ChI sequence emanating from $\nu = -1$. Different colours denote different flavours. Top: ChI (t, s) = (-3, -1). Bottom: how the experimentally observed sequence can be derived by selectively populating (middle) or emptying (bottom) subbands in a given flavour. c, Experimentally determined many-body Hofstadter spectrum. Each dot represents the extracted chemical potential at selected n. The dot density reflects the many-body density of states. Different colours map to states at different n and trace how their energies change upon flux insertion. The spectral gaps that correspond to parent ChIs/ $\nu_C = \pm 4$ zLLs are labelled.

Unexpected correlated ChIs and other distinctive features appear at high fields. Nearly all reports on hBN-unaligned samples show ChIs that only emanate away from the CNP with increasing B. In contrast, we observe a positive-sloped (t,s)=(1,-3) state that forms above $B\approx 6\,\mathrm{T}$. Similarly, a vertical incompressible (0,-2) state appears above $B\approx 9\,\mathrm{T}$. Neither of these states have been reported before, and they are striking because they represent reentrant behaviour in s as a function of ν and B. In addition, the s=-1 ChIs follow an unusual hierarchy of $t=\{-3,-2,-5,-7\}$ (in descending strength), whereas its electron counterpart has a sequence of $t=\{3,2,4,5\}$. Finally, we observe a ChI that extrapolates to a noninteger s=-1/2, indicative of translational symmetry breaking 13 . The phenomenology described above is largely reproduced in other independent regions of the sample (Extended Data Fig. 4) and is still robust at temperature $T=1.7\,\mathrm{K}$ (Extended Data Fig. 5).

The sequences of ChIs can be understood in the framework of correlation-driven flavour-polarized Hofstadter subbands^{13,14}. Starting with a single flavour at fixed *B*, the basic structure and Chern numbers of the Hofstadter subbands are fixed by theoretical

considerations^{35–39}. The experimentally observed zLL/ChI sequences suggest additional substructure, and we schematically illustrate an inferred phenomenological model in Fig. 2a. Theory predicts that the subbands extending from the superlattice band edge carry C=1, while near the CNP, C=2 subbands are expected due to the presence of two moiré valleys of the same helicity^{35–39}. However, we represent them as doublets of C=1 subbands to account for the aforementioned moiré valley splitting observed experimentally. Finally, the remaining subbands whose single-particle gaps are small compared with disorder and/or thermal broadening are combined into one large subband that contains the van Hove singularity (vHs). This large subband must carry C=-4 to satisfy the total C=0 constraint for the whole spectrum.

With multiple flavours and interflavour interaction, occupation of the Hofstadter subbands in Fig. 2a can be inequivalent for different flavours 13,14,16 , giving rise to broken-symmetry ChIs. The most prominent ChIs correspond to equal filling of an integer number of flavours up to the largest C=1/-1 gaps 13,14,16 . Additional broken-symmetry ChIs are formed by further filling or emptying

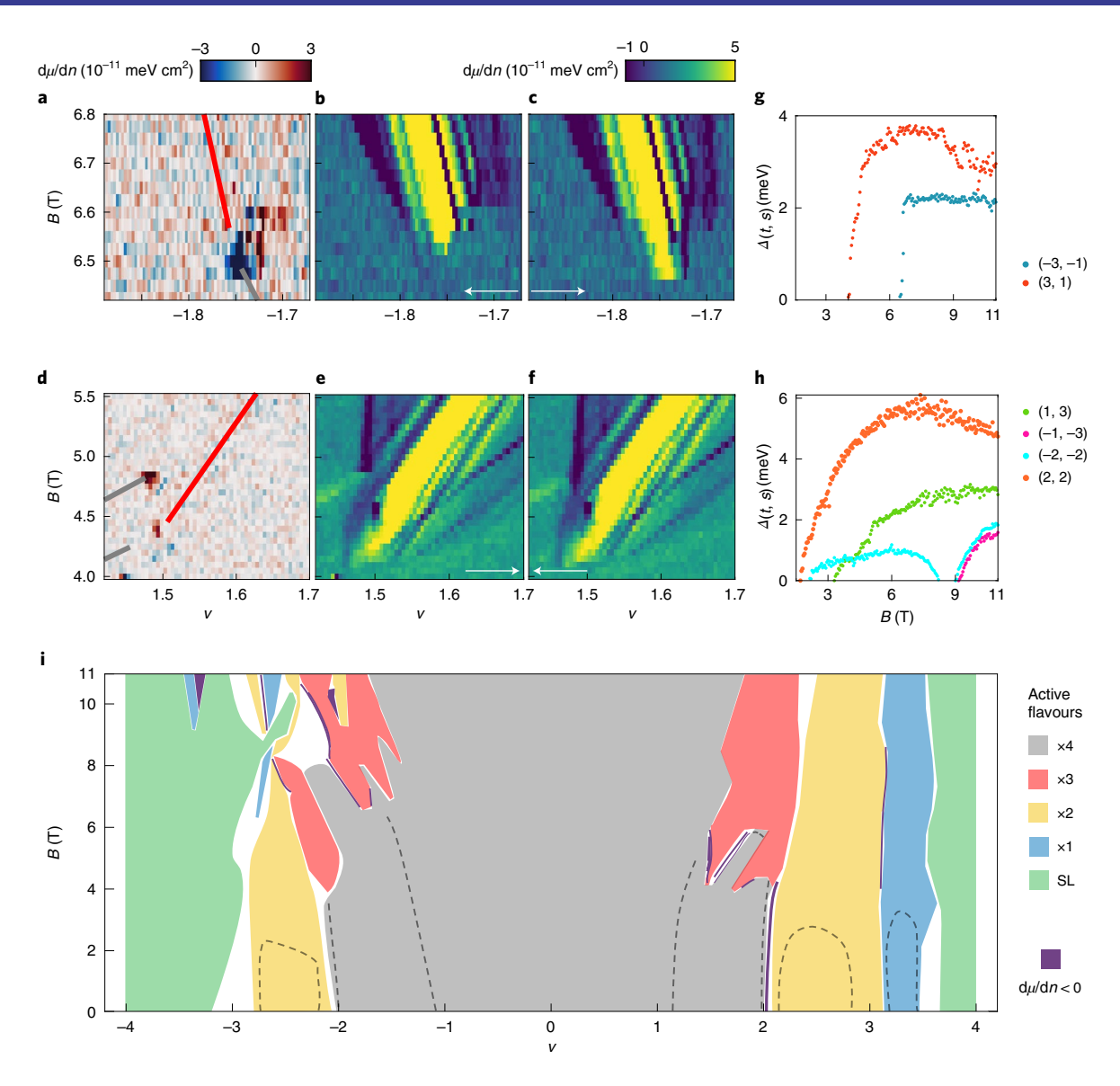


Fig. 3 | **First-order phase transitions and flavour phase diagram. a-c**, Hysteresis $d\mu/dn_{lec} - d\mu/dn_{dec}$ (a) derived from increasing (b) and decreasing (c) density sweeps near the onset of the (-3, -1) Chl. Red and grey lines in a show the positions of (-3, -1) and (-7, 0) states, respectively. White arrows indicate directions for tuning density. **d-f**, Hysteresis $d\mu/dn_{lec} - d\mu/dn_{dec}$ (d) derived from increasing (e) and decreasing (f) density sweeps near the (3, 1) onset transition. Red lines in **d** show the position of the (3, 1) state; the grey lines show the positions of the (8, 0) and (9, 0) states, respectively. **g,h**, Thermodynamic energy gaps of the predominant |s| + |t| = 4 sequence parent Chls as a function of B. **i**, Flavour occupation phase diagram of MATBG as a function of ν and ν and ν are denoted from the superlattice (SL) gap. Purple lines and areas denote regions where we observe negative $d\mu/dn$, indicating where phase transitions occur. Dashed lines indicate boundaries of the low-field sawtooth in $d\mu/dn$.

of additional subbands within the same active flavours. All the ChIs that we observe can be explained within this framework. A representative example that explains the experimentally observed ChI sequence emanating from s=-1 is illustrated in Fig. 2b. The most prominent, (-3, -1) state involves equal occupation of three flavours (Fig. 2b, top). Figure 2b (bottom) schematically shows how adding charge to a single moiré valley subband of one flavour produces a (-2, -1) state, whereas removing charge from the highest occupied doublet in one or two flavours leads to the (-5, -1) and (-7, -1) ChIs, respectively. A more comprehensive explanation of all the ChIs that we observe is detailed in Supplementary Section 6.

Our data indicate a delicate competition between different ChIs in the presence of single-particle and interaction-driven symmetry breaking. This is exemplified by the striking feature in Fig. 1e near $\nu = -8/3$ and B = 8.7 T and the corresponding region in Fig. 1d,

where different ChIs with s=-4, -3, -2 and -1 all intersect. The behaviour near this parameter range also shows strong spatial dependence (Extended Data Fig. 6). We therefore conclude that details such as small twist angle and strain variations can tip the balance between closely competing ChIs. These ChIs also compete with compressible states, and for the same reason, it is difficult to predict which ChIs will appear. We note that, although multiple combinations of subbands can often produce the right (t, s), those that require additional numbers of active flavours are likely energetically unfavourable, because they generate both large single-particle and interaction-energy penalties.

A key benefit of our measurement technique is that we can extract thermodynamic gaps and bandwidths by integrating $d\mu/dn$ to obtain $\mu(n, B)$. By selecting a number of equally spaced n, we can experimentally determine the many-body Hofstadter spectrum

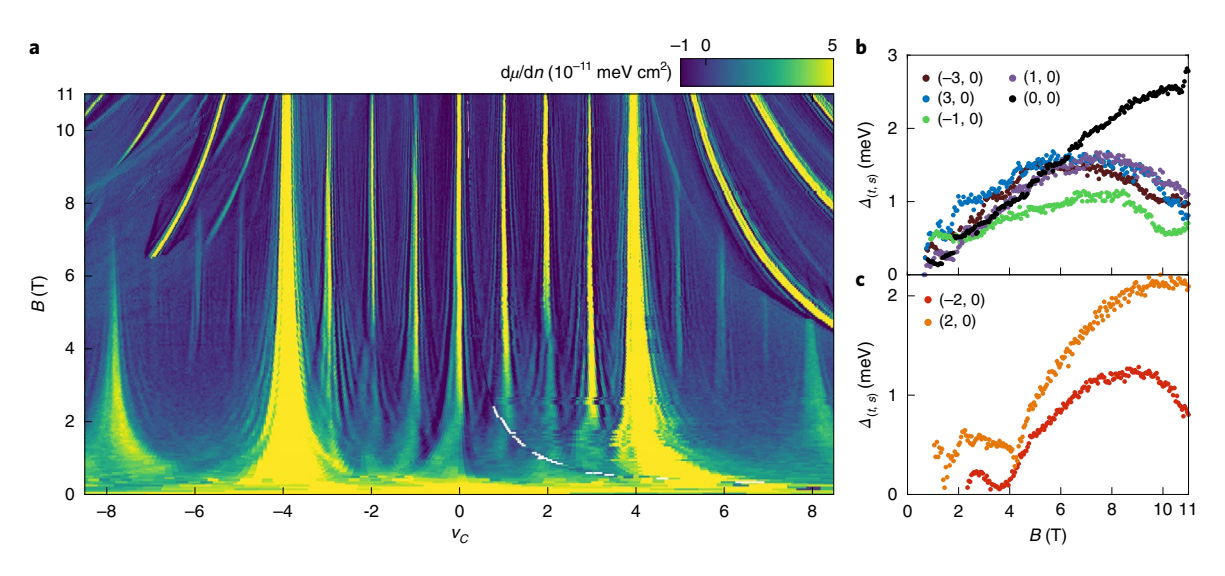


Fig. 4 | zLLs and moiré valley polarization. a, Measured $d\mu/dn$ in Fig. 1d replotted as a function of the zLL filling factor ν_c and B. **b,c**, Thermodynamic energy gaps of states at $\nu_c = 0$, ± 1 and ± 3 (**b**) and $\nu_c = \pm 2$ (**c**). The dips in the gaps of $\nu_c = \pm 2$ near 4T indicate LL crossings.

(Fig. 2c and Supplementary Section 5) based on the data in Fig. 1d (Extended Data Fig. 7 shows an analogous spectrum from another location). Each dot in the plotted spectrum represents one state of energy E at a given B. Hence, the density of dots represents the many-body density of states and can be compared with a numerically calculated Hofstadter spectrum. The overall shape of the spectrum generally agrees with continuum-model-based single-particle calculations³⁵⁻³⁸ which are characterized by the saturation of the $\nu_C = \pm 4$ zLL gaps and a reduction in total bandwidth with increasing B. While individual Hofstadter subbands are evident, their details differ from a simple replication of the single-particle spectrum due to the strong correlations present in MATBG. Most notably, we observe additional spectral gaps associated with broken-symmetry ChIs at high magnetic fields as well as LL-like ChIs emerging from $\nu = \pm 2$ at moderate fields. The spectrum also exhibits a recurring pattern of dense points which reflect vHs-like features where the flavour phase transitions occur (Fig. 2c, black arrows).

The data in Fig. 2c represent the first quantitative measurement of an interacting Hofstadter spectrum. The resulting spectrum is distinct from typical tunnelling spectroscopy measurements of density of states in which a tunnel bias is swept while maintaining fixed density. This is because our measurement always probes at the Fermi energy and is therefore sensitive to many-body effects at all plotted energies, whereas electrons generally tunnel above or below the Fermi energy in tunnelling spectroscopies. Another advantage of our approach is that it avoids tip-induced doping and soft Coulomb gaps that can be present in tunnelling experiments.

First-order polarization transitions and flavour phase diagram

Our measurements provide detailed information about the phase diagram of flavour occupancy as a function of ν and B. We first discuss the abrupt appearance of the ChIs at $(\pm 3, \pm 1)$. Theory predicts that these phase transitions can be first order³³, and transport experiments have indeed shown abrupt onset¹³ and hysteresis from other ChIs emanating from $\nu = 1$ (Ref. ⁵). In our experiment, these states form abruptly in the middle of a zLL fan and are flanked by sharply negative $d\mu/dn$ (Fig. 3b,c,e,f). Their energy gaps saturate soon after they form (Fig. 3g), whereas the gaps of all other ChIs exhibit a more gradual increase near their onset (Fig. 3h, and Supplementary Section 4 for details of thermodynamic gap extraction). Strikingly, we observe hysteresis in $d\mu/dn$ near the critical B and ν of the

(± 3 , ± 1) states, which provides the first direct thermodynamic evidence of a first-order phase transition between unpolarized/partially polarized zLLs and broken-symmetry ChIs. Hysteresis is apparent both when ν is modified at fixed B (Fig. 3a-f) and when B is adjusted at fixed ν (Extended Data Fig. 8). Interestingly, the hysteretic region coincides with the intersection point of zLLs with (± 3 , ± 1) and is not ubiquitous in the entire negative $d\mu/dn$ regions (Fig. 3a,d). We do not observe hysteresis near these transitions at 1.7 K, and no hysteresis was evident in any other parts of the phase diagram even at base temperature. However, we cannot preclude that other phase transitions are also first order but masked by disorder and/or thermal broadening.

We observe multiple additional features where $d\mu/dn < 0$, many of which occur between incompressible states. Negative $d\mu/dn$ can be a hallmark of interaction-driven ground-state phase transitions, where the free energies of different electronic states cross^{42,43}. In MATBG, these crossings correspond to flavour polarization transitions, and based on the locations of the negative $d\mu/dn$ features, we can construct a phase diagram that characterizes the number of active flavours in the entire ν -B plane (Fig. 3i and Supplementary Section 8). This phase diagram, which is a central result of this paper, reveals an intricate pattern of phase boundaries, including reentrant behaviour in the number of active flavours. The detailed slopes and curvatures of the negative compressibility features are likely related to the underlying spin/orbital moments of the adjacent phases. While a full explanation of their form lies beyond the scope of this work, our results inform and constrain microscopic theories that address specific spin and valley ordering throughout the phase diagram.

Our data also clarify the evolution between the characteristic sawtooth in $d\mu/dn$ at B=0, which persists to finite fields, and the high-field regime of flavour-polarized Hofstadter subbands. The zLLs and low-field ChIs with |s|=2 and 3 coexist with the sawtooth over a range of densities. An estimated boundary of the sawtooth is superimposed on top of the flavour phase diagram in Fig. 3i (dashed lines). The continuation of the sawtooth in nonzero B and its coexistence with zLLs/ChIs can be simultaneously understood by considering a Stoner mechanism in the Hofstadter subbands near the CNP. This gives rise to a hierarchy of transitions. Namely, Stoner transitions that maintain the same number of active flavours can generate quantum Hall (flavour) ferromagnets and give rise to the observed sequence of zLLs and low-field ChIs. Upon increasing density

toward the vHs, these give way to transitions which completely reset the number of active flavours, terminate the ChIs and can be understood as continuations of the cascade of transitions at B=0 (ref. 9). Interestingly, this mechanism was recently reported in a compressibility measurement on rhombohedral trilayer graphene⁴³, hinting at the universality of the polarizing mechanism in correlated itinerant electronic systems with multiple internal degrees of freedom.

zLLs, ChI degeneracies and moiré valley polarization

The evolution of the zLLs with B provides further insight into the symmetry breaking present in our device. Figure 4a shows the zLLs plotted as a function of ν_C and B. We resolve all zLLs within $-4 < \nu_C < 4$. Surprisingly, both even and odd integers emerge at similar magnetic fields and have similar gap sizes (Fig. 4b,c). This does not show obvious angle dependence over a large spatial region that encompasses a variety of twist angles (Extended Data Figs. 2 and 4). Although singly degenerate zLLs have been reported previously^{4,13-19,41,44}, no consensus has been reached on the driving mechanism. A second important experimental finding is the dips in the energy gaps at $\nu_C = \pm 2$ that occur near B = 4 T (Fig. 4c). This behaviour indicates zLL crossings and is also reproduced in multiple locations in the sample (Extended Data Figs. 4 and 9).

Several theoretical mechanisms that could potentially lift the zLL degeneracy have been proposed, and we consider each in turn below. The density dependence of compressibility and the magnitudes of the energy gaps at $\nu_C = \pm 4$ are consistent with a Dirac dispersion near the CNP, rendering the scenario where band extrema occur at the centre of the mBZ unlikely ¹⁶. Two types of symmetry breaking can lift the zLL degeneracy ^{29,38}: C_{3z} and M_y . Breaking C_{3z} alone can halve the zLL degeneracy but is predicted to involve vHs physics and occur at finite B. Moreover, no level crossings are expected in this scenario. We therefore conclude that M_y breaking is the most likely explanation for the observed zLL behaviour ¹⁶.

In MATBG, M_{ν} can be broken by external effects such as heterostrain^{29,45,46}, and can also be caused or further enhanced by interactions⁴⁷. This would energetically distinguish the two Dirac nodes^{29,45,46} in each mBZ by an amount Δ_{ν} (Extended Data Fig. 10a). Two quartets of zLLs are expected to emanate from each respective Dirac cone, with correlation gaps that scale linearly with applied field due to interflavour repulsion $U\nu_i\nu_i$ between flavours i and j (ref. 33) (Supplementary Section 9). Extended Data Fig. 10b illustrates the corresponding evolution of the zLL free energies, which results in crossings16 between states associated with different moiré valleys. This naturally explains the closing and reopening of the $\nu_c = \pm 2$ gaps as a function of B, and also matches the observation that the odd ν_c gaps have similar magnitudes at high fields. Within this model, the effective U can be extracted from the B dependence of the zLL gaps (Fig. 4b,c) to be ~10 meV (Supplementary Section 9), which is consistent with estimates from earlier thermodynamic measurements^{11,14}. Other crossings are predicted but are not apparent in our data. Their absence can be explained by differences in interflavour splitting which could push them to fields below our experimental resolution (Extended Data Fig. 10d,e and Supplementary Section 9). We note that this mechanism does not require the two Dirac nodes to reside at the mBZ corners and is therefore still valid in the presence of C_{3z} breaking. Furthermore, such moiré valley splitting also provides a natural explanation for the singly degenerate sequence of ChIs emanating from $\nu = 3$, which cannot otherwise be reconciled with the presence of two degenerate moiré valleys contributing to the Hofstadter spectrum⁴⁸.

Conclusion

We have experimentally determined the interacting Hofstadter spectrum and phase diagram of flavour occupancy in MATBG and shown that a unifying flavour symmetry-breaking mechanism can capture the physics at multiple energy and field scales. A microscopic understanding of the specific spin and valley ordering in various regions of the phase diagram remains an exciting open question to be explored, and the close competition between ground states that we observe suggests that external tuning, for example, by strain, could be used as a control knob to switch between different correlated and topological ground states. More generally, we anticipate that the methods demonstrated here could be applied to map the phase diagrams and probe Hofstadter physics across the broad and rapidly growing set of strongly correlated moiré systems (3,49,50).

Online content

Any methods, additional references, Nature Research reporting summaries, source data, extended data, supplementary information, acknowledgements, peer review information; details of author contributions and competing interests; and statements of data and code availability are available at https://doi.org/10.1038/s41567-022-01589-w.

Received: 18 August 2021; Accepted: 17 March 2022; Published online: 25 April 2022

References

- Bistritzer, R. & MacDonald, A. H. Moiré bands in twisted double-layer graphene. Proc. Natl Acad. Sci. USA 108, 12233–12237 (2011).
- Cao, Y. et al. Correlated insulator behavior at half-filling in magic-angle graphene superlattices. *Nature* 556, 80–84 (2018).
- 3. Cao, Y. et al. Unconventional superconductivity in magic-angle graphene superlattices. *Nature* **556**, 43–50 (2018).
- 4. Yankowitz, M. et al. Tuning superconductivity in twisted bilayer graphene. *Science* **363**, 1059–1064 (2019).
- Lu, X. et al. Superconductors, orbital magnets and correlated states in magic-angle bilayer graphene. *Nature* 574, 653–657 (2019).
- Sharpe, A. L. et al. Emergent ferromagnetism near three-quarters filling in twisted bilayer graphene. Science 365, 605–608 (2019).
- Serlin, M. et al. Intrinsic quantized anomalous Hall effect in a moiré heterostructure. Science 367, 900–903 (2020).
- Cao, Y. et al. Nematicity and competing orders in superconducting magic-angle graphene. Science 372, 264–271 (2021).
- Zondiner, U. et al. Cascade of phase transitions and Dirac revivals in magic-angle graphene. *Nature* 582, 203–208 (2020).
- Wong, D. et al. Cascade of electronic transitions in magic-angle twisted bilayer graphene. *Nature* 582, 198–202 (2020).
- 11. Saito, Y. et al. Isospin Pomeranchuk effect in twisted bilayer graphene. *Nature* **592**, 220–224 (2021).
- Rozen, A. et al. Entropic evidence for a Pomeranchuk effect in magic-angle graphene. Nature 592, 214–219 (2021).
- Saito, Y. et al. Hofstadter subband ferromagnetism and symmetry-broken Chern insulators in twisted bilayer graphene. Nat. Phys. 17, 478–481 (2021).
- Park, J. M., Cao, Y., Watanabe, K., Taniguchi, T. & Jarillo-Herrero, P. Flavour Hund's coupling, Chern gaps and charge diffusivity in moiré graphene. Nature 592, 43–48 (2021).
- Nuckolls, K. P. et al. Strongly correlated Chern insulators in magic-angle twisted bilayer graphene. Nature 588, 610–615 (2020).
- Choi, Y. et al. Correlation-driven topological phases in magic-angle twisted bilayer graphene. *Nature* 589, 536–541 (2021).
- Das, I. et al. Symmetry-broken Chern insulators and Rashba-like Landau-level crossings in magic-angle bilayer graphene. *Nat. Phys.* https://doi. org/10.1038/s41567-021-01186-3 (2021).
- Wu, S., Zhang, Z., Watanabe, K., Taniguchi, T. & Andrei, E. Y. Chern insulators, van Hove singularities and topological flat bands in magic-angle twisted bilayer graphene. *Nat. Mater.* 20, 488–494 (2021).
- Tomarken, S. L. et al. Electronic compressibility of magic-angle graphene superlattices. *Phys. Rev. Lett.* 123, 046601 (2019).
- Pierce, A. et al. Unconventional sequence of correlated Chern insulators in magic-angle twisted bilayer graphene. Nat. Phys. 17, 1210–1215 (2021).
- Xie, Y. et al. Spectroscopic signatures of many-body correlations in magic-angle twisted bilayer graphene. *Nature* 572, 101–105 (2019).
- Kerelsky, A. et al. Maximized electron interactions at the magic angle in twisted bilayer graphene. *Nature* 572, 95–100 (2019).
- Jiang, Y. et al. Charge order and broken rotational symmetry in magic-angle twisted bilayer graphene. Nature 573, 91–95 (2019).
- Choi, Y. et al. Electronic correlations in twisted bilayer graphene near the magic angle. *Nat. Phys.* 15, 1174–1180 (2019).
- Saito, Y., Ge, J., Watanabe, K., Taniguchi, T. & Young, A. F. Independent superconductors and correlated insulators in twisted bilayer graphene. *Nat. Phys.* 16, 926–930 (2020).

- 26. Stepanov, P. et al. Untying the insulating and superconducting orders in magic-angle graphene. *Nature* **583**, 375–378 (2020).
- Liu, X. et al. Tuning electron correlation in magic-angle twisted bilayer graphene using Coulomb screening. Science 371, 1261–1265 (2021).
- Stepanov, P. et al. Competing zero-field Chern insulators in superconducting twisted bilayer graphene. Phys. Rev. Lett. 127, 197701 (2021).
- Po, H. C., Zou, L., Vishwanath, A. & Senthil, T. Origin of Mott insulating behavior and superconductivity in twisted bilayer graphene. *Phys. Rev. X* 8, 031089 (2018).
- Bultinck, N. et al. Ground state and hidden symmetry of magic-angle graphene at even integer filling. Phys. Rev. X 10, 031034 (2020).
- Kang, J. & Vafek, O. Strong coupling phases of partially filled twisted bilayer graphene narrow bands. *Phys. Rev. Lett.* 122, 246401 (2019).
- Liu, J., Liu, J. & Dai, X. Pseudo Landau level representation of twisted bilayer graphene: band topology and implications on the correlated insulating phase. *Phys. Rev. B* 99, 155415 (2019).
- 33. Lian, B. et al. Twisted bilayer graphene. IV. Exact insulator ground states and phase diagram. *Phys. Rev. B* **103**, 205414 (2021).
- Hofstadter, D. R. Energy levels and wave functions of Bloch electrons in rational and irrational magnetic fields. *Phys. Rev. B* 14, 2239–2249 (1976).
- Bistritzer, R. & MacDonald, A. H. Moiré butterflies in twisted bilayer graphene. Phys. Rev. B 84, 035440 (2011).
- 36. Moon, P. & Koshino, M. Energy spectrum and quantum Hall effect in twisted bilayer graphene. *Phys. Rev. B* **85**, 195458 (2012).
- 37. Hejazi, K., Liu, C. & Balents, L. Landau levels in twisted bilayer graphene and semiclassical orbits. *Phys. Rev. B* **100**, 035115 (2019).
- Zhang, Y.-H., Po, H. C. & Senthil, T. Landau level degeneracy in twisted bilayer graphene: role of symmetry breaking. *Phys. Rev. B* 100, 125104 (2019).
- Lian, B., Xie, F. & Bernevig, B. A. Landau level of fragile topology. *Phys. Rev.* B 102, 041402 (2020).

- Wannier, G. H. A result not dependent on rationality for Bloch electrons in a magnetic field. *Phys. Status Solidi B* 88, 757–765 (1978).
- 41. Uri, A. et al. Mapping the twist-angle disorder and Landau levels in magic-angle graphene. *Nature* **581**, 47–52 (2020).
- Eisenstein, J. P., Pfeiffer, L. N. & West, K. W. Negative compressibility of interacting two-dimensional electron and quasiparticle gases. *Phys. Rev. Lett.* 68, 674–677 (1992).
- 43. Zhou, H. et al. Half-and quarter-metals in rhombohedral trilayer graphene. *Nature* **598**, 429–433 (2021).
- Arora, H. S. et al. Superconductivity in metallic twisted bilayer graphene stabilized by WSe, *Nature* 583, 379–384 (2020).
- Bi, Z., Yuan, N. F. Q. & Fu, L. Designing flat bands by strain. *Phys. Rev. B* 100, 035448 (2019).
- Parker, D. E., Soejima, T., Hauschild, J., Zaletel, M. P. & Bultinck, N. Strain-induced quantum phase transitions in magic-angle graphene. *Phys. Rev. Lett.* 127, 027601 (2021).
- Huang, K. S., Han, Z., Kivelson, S. A. & Yao, H. Pair-density-wave in the strong coupling limit of the Holstein-Hubbard model. *npj Quantum Mater.* 7, 17 (2022).
- Kang, J., Bernevig, B. A. & Vafek, O. Cascades between light and heavy fermions in the normal state of magic angle twisted bilayer graphene. Preprint at https://arxiv.org/abs/2104.01145 (2021).
- 49. Kennes, D. M. et al. Moiré heterostructures as a condensed-matter quantum simulator. *Nat. Phys.* **17**, 155–163 (2021).
- Chen, G. et al. Evidence of a gate-tunable Mott insulator in a trilayer graphene moiré superlattice. Nat. Phys. 15, 237–241 (2019).

Publisher's note Springer Nature remains neutral with regard to jurisdictional claims in published maps and institutional affiliations.

© The Author(s), under exclusive licence to Springer Nature Limited 2022

Methods

Device fabrication. The MATBG stack was fabricated using a standard dry transfer technique 51 . A monolayer graphene flake was precut by using a conductive atomic force microscopy probe 26,27,50 in contact mode, with an alternating-current (AC) excitation of $10\,\rm V_{p-p}$ at 50 kHz, to minimize tearing-induced strain. The two isolated flakes were rotated $1.15^{\rm o}$ relative to each other before stacking and encapsulated by top (27 nm) and bottom (40 nm) hBN. Few-layer graphite was used as the bottom gate. Metal electrodes were subsequently patterned using standard e-beam lithography techniques to form edge contacts 51 .

Scanning SET measurements. The SET sensor was fabricated by evaporating aluminium onto the apex of a pulled quartz rod. The size of the apex, and thus the lateral dimension of the SET, is estimated to be 50–80 nm. It was brought to <50 nm above the MATBG sample surface, resulting in an overall spatial resolution of about 100 nm. The scanning SET measurements were performed in a Unisoku USM 1300 scanning probe microscope with a customized microscope head. An AC excitation of $V_{\rm g} = 4-8\,{\rm mV}$ at $f_{\rm g} = 911.999\,{\rm Hz}$ was applied to the back gate, and an AC excitation $V_{2d} = 1\,{\rm mV}$ at $f_{2d} = 773.777\,{\rm Hz}$ was applied to the sample. We then measured the inverse compressibility $\alpha I_y I_{2d}$, where $I_{\rm g}$ and I_{2d} are demodulated from the SET current through the SET probe using standard lock-in techniques. A direct-current (DC) offset voltage V_{2d} is further applied to the sample to maintain maximum sensitivity of the SET and minimize tip-induced doping (Supplementary Section 2). All data presented are taken at 330 mK unless otherwise specified.

Gate capacitance and twist angle determination. The sample gate capacitance (conversion between density and applied gate voltage) was calibrated by measuring the slope of zLLs, which yielded a value consistent with geometric considerations. The twist angle is then given by the relation $\theta(\mathbf{r}) = (\sqrt{3}n_s(\mathbf{r})/8)^{1/2}$ where $a=0.246\,\mathrm{nm}$ is graphene's lattice constant and $n_s(\mathbf{r})$ is the carrier density at full filling.

Background subtraction. A finite geometric capacitance between the tip and back-gate electrode can contribute to an overall constant spurious background in measured $d\mu/dn$. To estimate this parasitic signal, we compare the measured $d\mu/dn$ of the higher dispersive bands at $|\nu| > 4$ in the contact area and at the centre of the device, where the twist angle is slightly larger (~1.14–1.2°). The latter has a lower background because of better screening of the back gate and larger separation from its electrode. We found a small but finite difference of $8\times 10^{-12}\,\mathrm{meV}\,\mathrm{cm}^2$, which we subtract from all the presented data. Differences in $d\mu/dn$ from differences in the details of the dispersive bands are small and will therefore not affect our observations. The background contribution is still likely to be finite even at the centre of the sample given the small size of the device, so we conclude that we are likely undersubtracting the true parasitic background signal. This will enlarge the measured bandwidth by a small amount (<5%) but has a negligible effect on the extracted gap sizes.

Scanning MIM measurement. MIM measurements were performed in a ³He cryostat with a 12 T superconducting magnet and custom scanner incorporating Attocube nanopositioners. The MIM probe, an etched tungsten wire, was attached to a quartz tuning fork for topographic sensing, and scans were taken with the tip held approximately 20 nm above the sample's surface. MIM measures changes in admittance between the tip and sample at GHz frequencies, which can be related to changes in local conductivity and permittivity in the sample. The measurements reported here were carried out at 6.8 GHz. At GHz frequencies, the tip and sample are strongly capacitively coupled, enabling subsurface sensing without requiring additional electrical contacts on the sample. MIM operates in the near-field limit,

and the spatial resolution is dictated by the tip diameter (~100 nm) rather than the microwave wavelength.

Data availability

The data that support the findings of this study are available from the corresponding author upon reasonable request. Source data are provided with this paper.

Code availability

The codes that support the findings of this study are available from the corresponding author upon reasonable request.

References

 Wang, L. et al. One-dimensional electrical contact to a two-dimensional material. Science 342, 614–617 (2013).

Acknowledgements

We thank D. Goldhaber-Gordon and O. Vafek for helpful discussions. This work was supported by the QSQM, an Energy Frontier Research Center funded by the US Department of Energy (DOE), Office of Science, Basic Energy Sciences (BES), under award no. DE-SC0021238. B.E.F. acknowledges a Stanford University Terman Fellowship and an Alfred P. Sloan Foundation Fellowship. K.W. and T.T. acknowledge support from the Elemental Strategy Initiative conducted by MEXT, Japan (grant no. JPMXP0112101001) and JSPS KAKENHI (grant no. JP20H00354). S.A.K. acknowledges support from the Department of Energy, Office of Basic Energy Sciences, under contract no. DEAC02-76SF00515. B.A.F. acknowledges a Stanford Graduate Fellowship. M.E.B. acknowledges support from the Marvin Chodorow Postdoctoral Fellowship of the Applied Physics Department, Stanford University. Y.S. was supported by the Gordon and Betty Moore Foundation's EPiQS Initiative through grants GBMF 4302 and GBMF 8686. P.P. acknowledges partial support from NSF grant DMR-2111379. Part of this work was performed at the Stanford Nano Shared Facilities (SNSF), supported by the National Science Foundation under award ECCS-2026822.

Author contributions

J.Y., B.A.F. and B.E.F. designed and conducted the scanning SET experiments. M.E.B. and Z.-X.S. designed and conducted the MIM experiments. B.A.F. fabricated the sample. Z.H., Y.S., S.A.K. and P.P. contributed to theoretical analysis. K.W. and T.T. provided hBN crystals. All authors participated in discussions and in writing of the manuscript.

Competing interests

Z.-X.S. is a co-founder of PrimeNano Inc., which licensed the MIM technology from Stanford University for commercial instruments.

Additional information

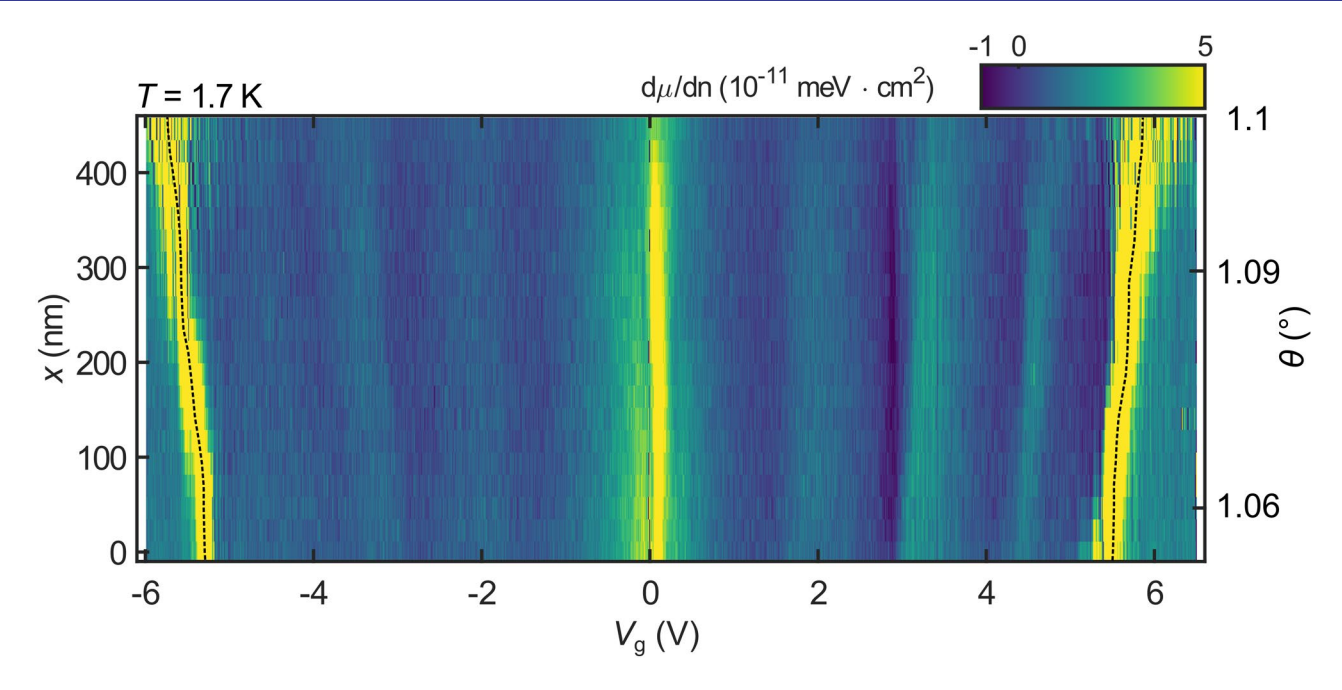
 $\textbf{Extended data} \ \text{is available for this paper at https://doi.org/10.1038/s41567-022-01589-w.}$

Supplementary information The online version contains supplementary material available at https://doi.org/10.1038/s41567-022-01589-w.

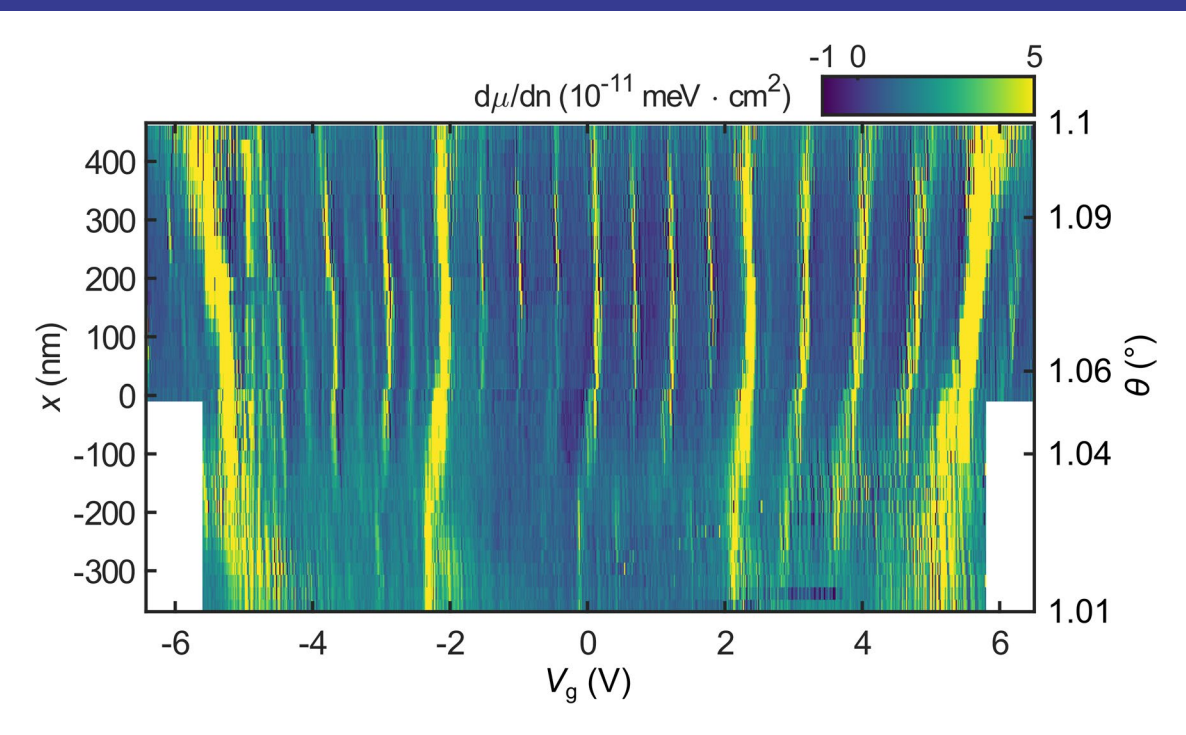
Correspondence and requests for materials should be addressed to Benjamin E. Feldman.

Peer review information *Nature Physics* thanks the anonymous reviewers for their contribution to the peer review of this work

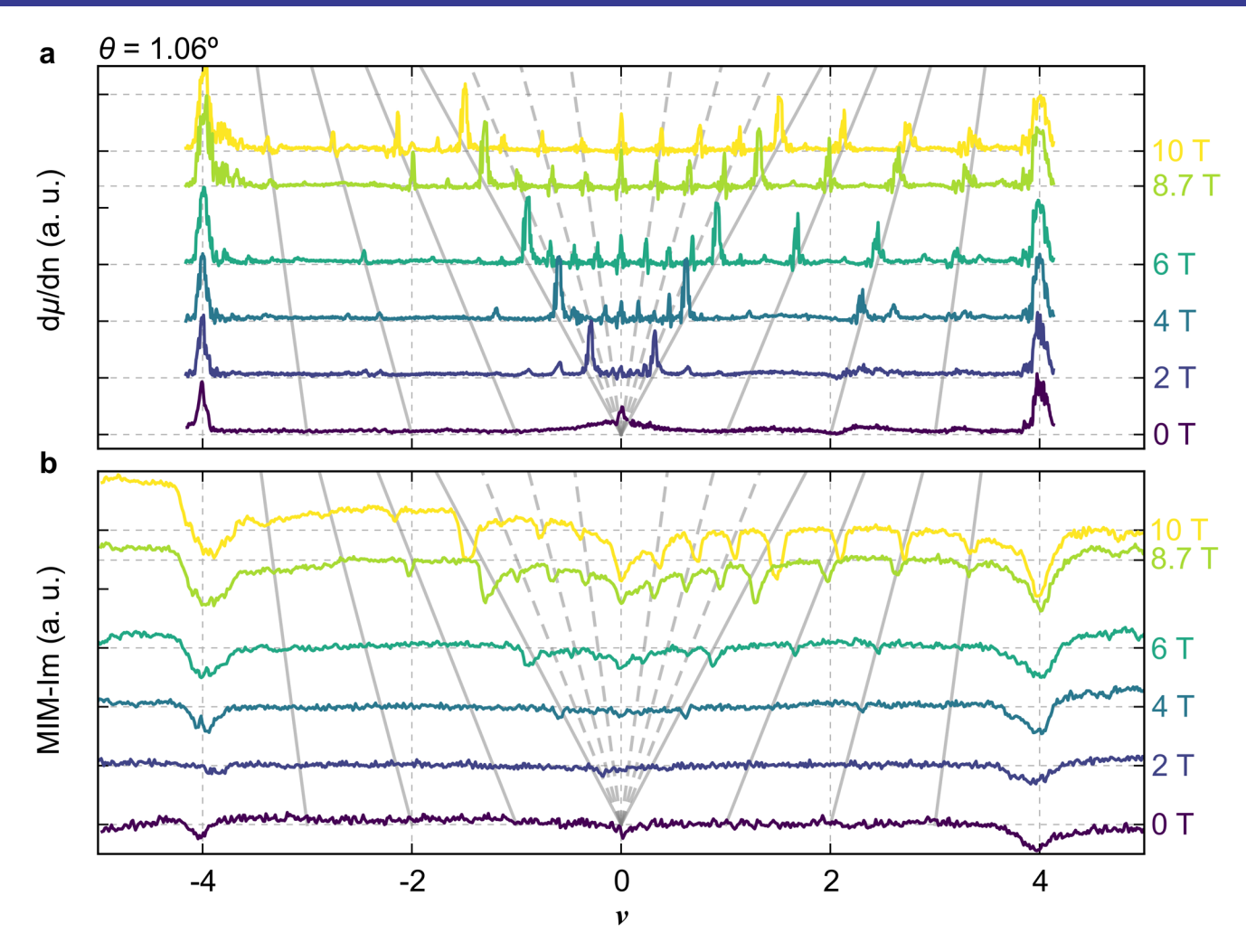
Reprints and permissions information is available at www.nature.com/reprints.



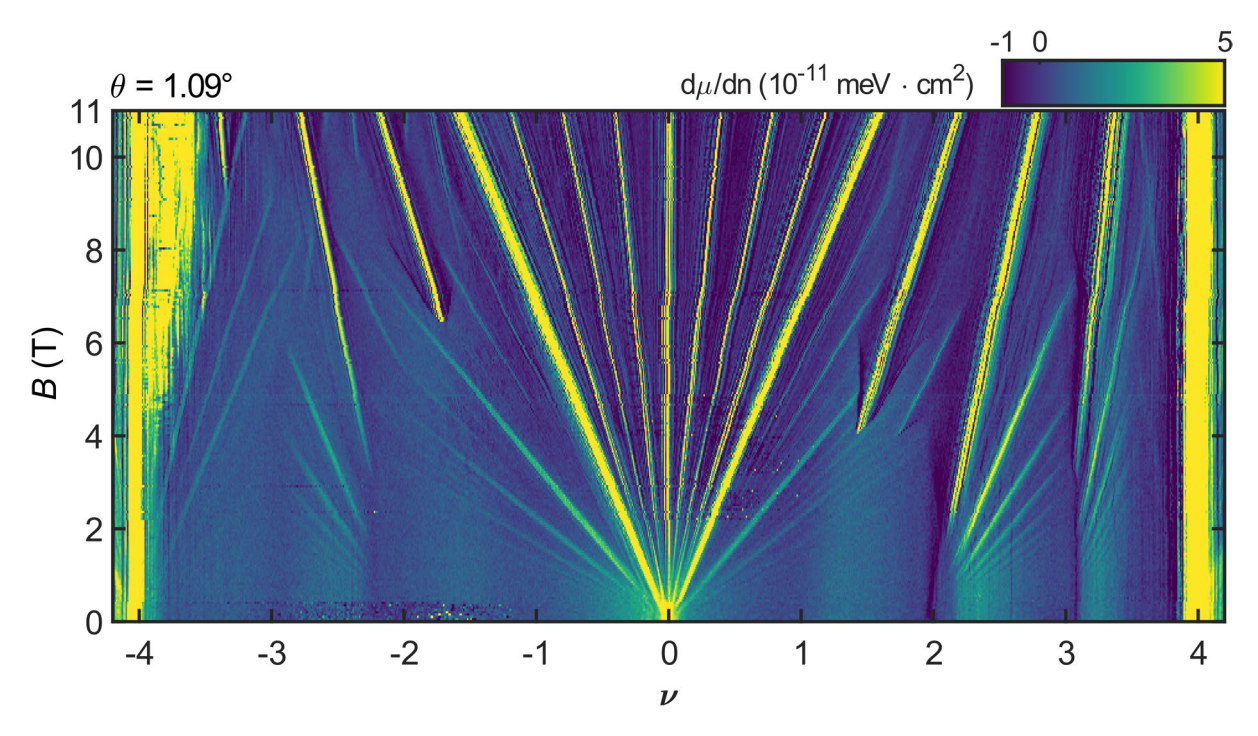
Extended Data Fig. 1 | Spatial dependence of electronic compressibility at zero field. Linecut of $d\mu/dn$ as a function of gate voltage (V_g) measured along a line in the top left contact area of the device shown in Fig. 1a. The Landau fans shown in Fig. 1 and Extended Data Fig. 4 are taken at x = 40 nm and x = 300 nm, respectively. The sawtooth pattern on the electron side generically exhibits a larger amplitude and negative $d\mu/dn$ at the $\nu = 2$ transition. Dashed lines denote gate voltages corresponding to $\nu = \pm 4$.



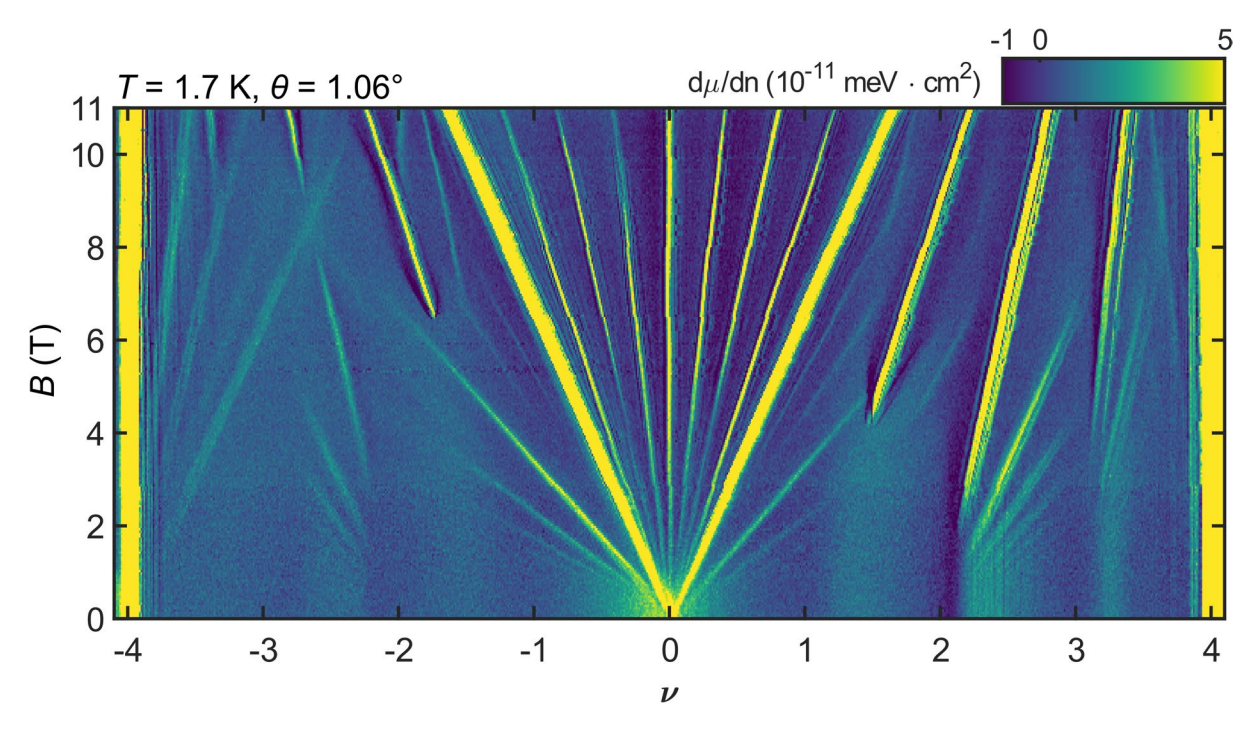
Extended Data Fig. 2 | Spatial dependence of zLL and Chls. Linecut of $d\mu/dn$ at 11 T. The positions with x > 0 correspond to those shown in Extended Data Fig. 1. While the overall strengths of the broken-symmetry zLLs is spatially dependent, those at odd integers have comparable strengths to those at even integers independent of position.



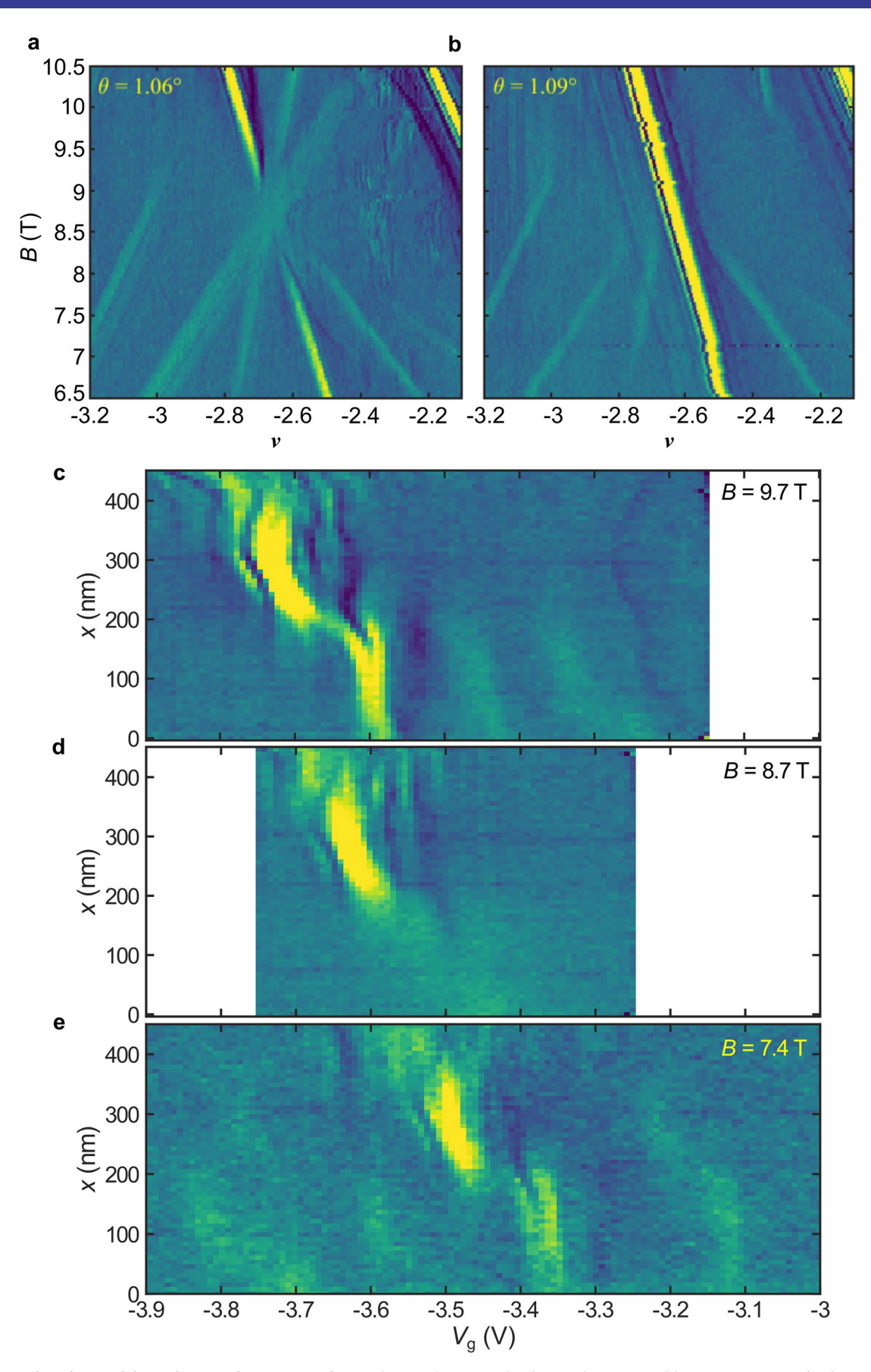
Extended Data Fig. 3 | Comparison of inverse electronic compressibility and MIM measurements. Selected $d\mu/dn$ measurements as a function of moiré filling factor ν at different perpendicular magnetic fields reproduced from Fig. 1d. The curves are vertically spaced according to the applied magnetic field and the grey lines indicate the field dependence of the incompressible states identified in Fig. 1e. **b**, MIM measurements of the local conductivity at the same sample position as a function of ν and at the same magnetic fields. A decrease in MIM-Im corresponds to a decrease in conductivity confirming the main ChI and zLLs are associated with local resistive behavior. The MIM measurements were taken at $T=450\,\text{mK}$.



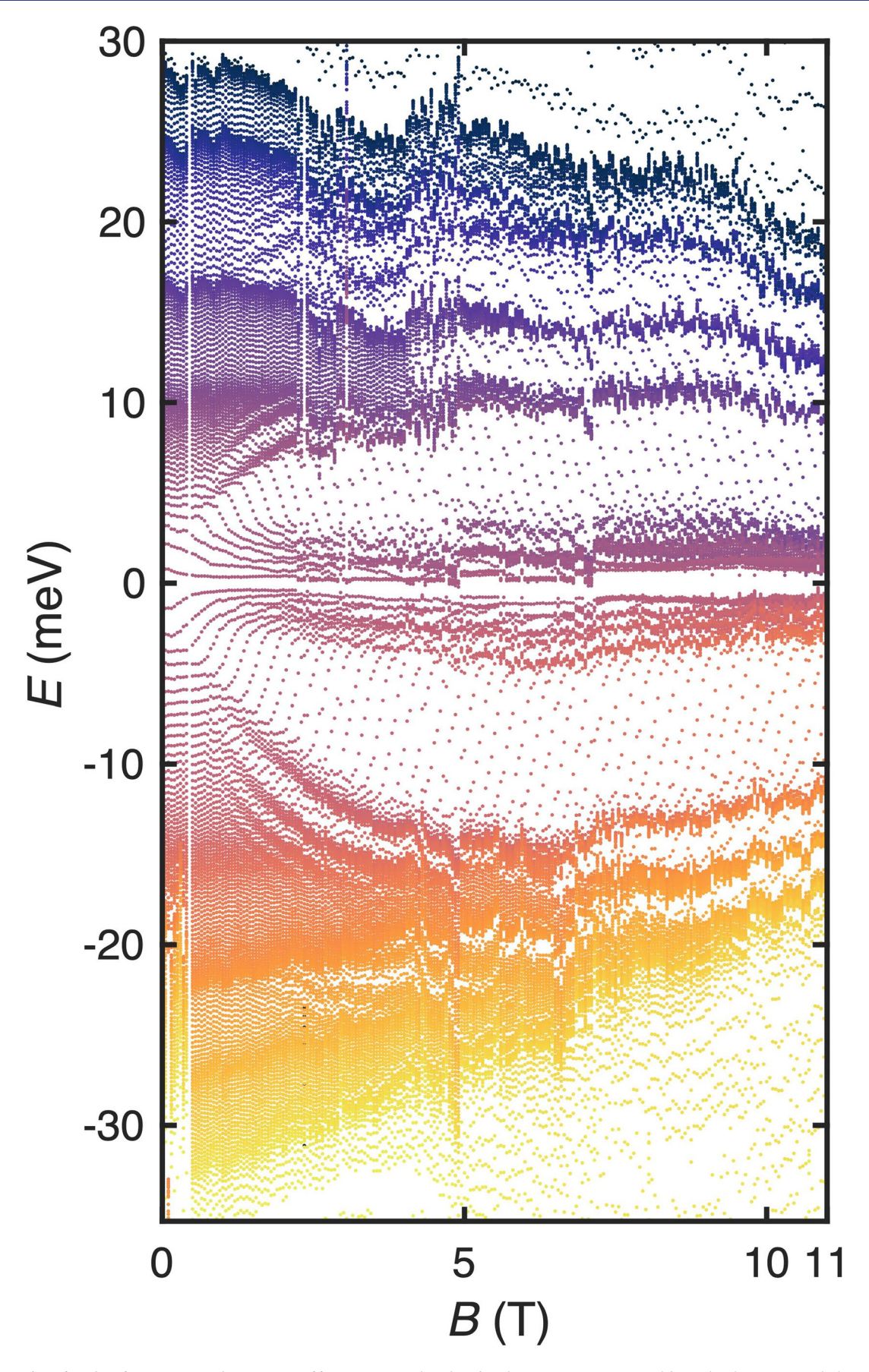
Extended Data Fig. 4 | Landau fan of Chls at a second location. $d\mu/dn$ measured at a second location (blue dot in Fig. 1a) with twist angle $\theta = 1.09^{\circ}$ showing qualitatively similar Chls/zLLs sequences and phase boundaries as in Fig. 1d.



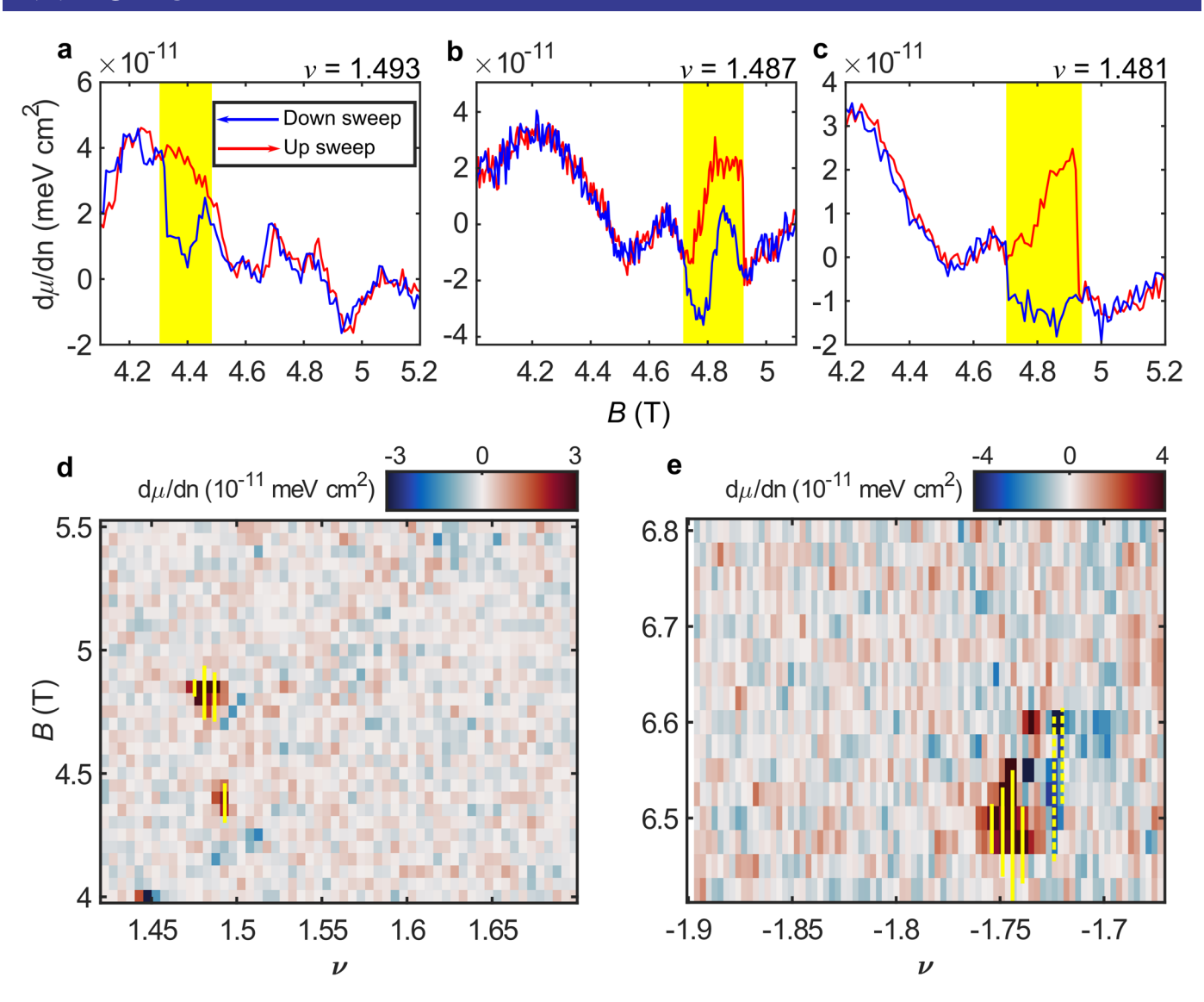
Extended Data Fig. 5 | Landau fan at higher temperature. $d\mu/dn$ measured at the location of Fig. 1d at temperature T=1.7 K. The Chls/zLLs and negative $d\mu/dn$ features are thermally broadened and weakened, but the qualitative pattern is unchanged. Interestingly, negative $d\mu/dn$ features that mark phase transitions appear closer to the adjacent incompressible states.



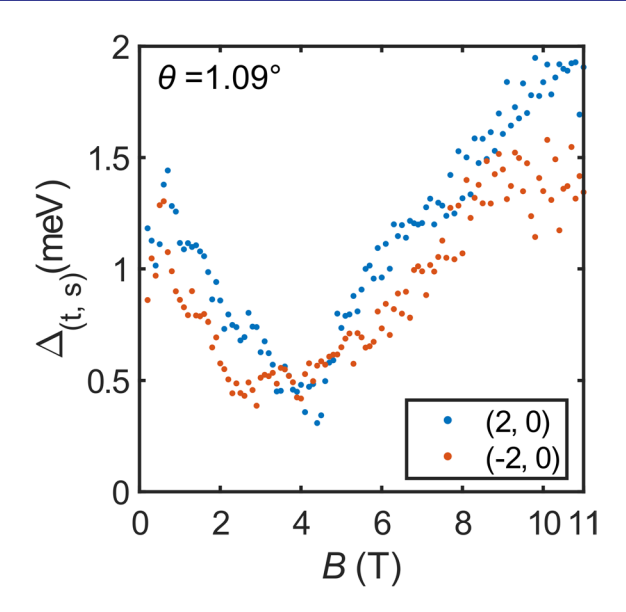
Extended Data Fig. 6 | Spatial dependence and competing Chls. Higher resolution Landau fans in the vicinity of ($\nu = -8/3$, B = 8.7 T) taken in the locations of Fig. 1d and Extended Data Fig. 4. The pattern of dominant Chls and detailed regions of negative $d\mu/dn$ are distinct in each location. **c-e**, Spatial linecuts (same trajectory as in Extended Data Fig. 1) taken at B = 9.4, 8.7, and 7.4 T, respectively.



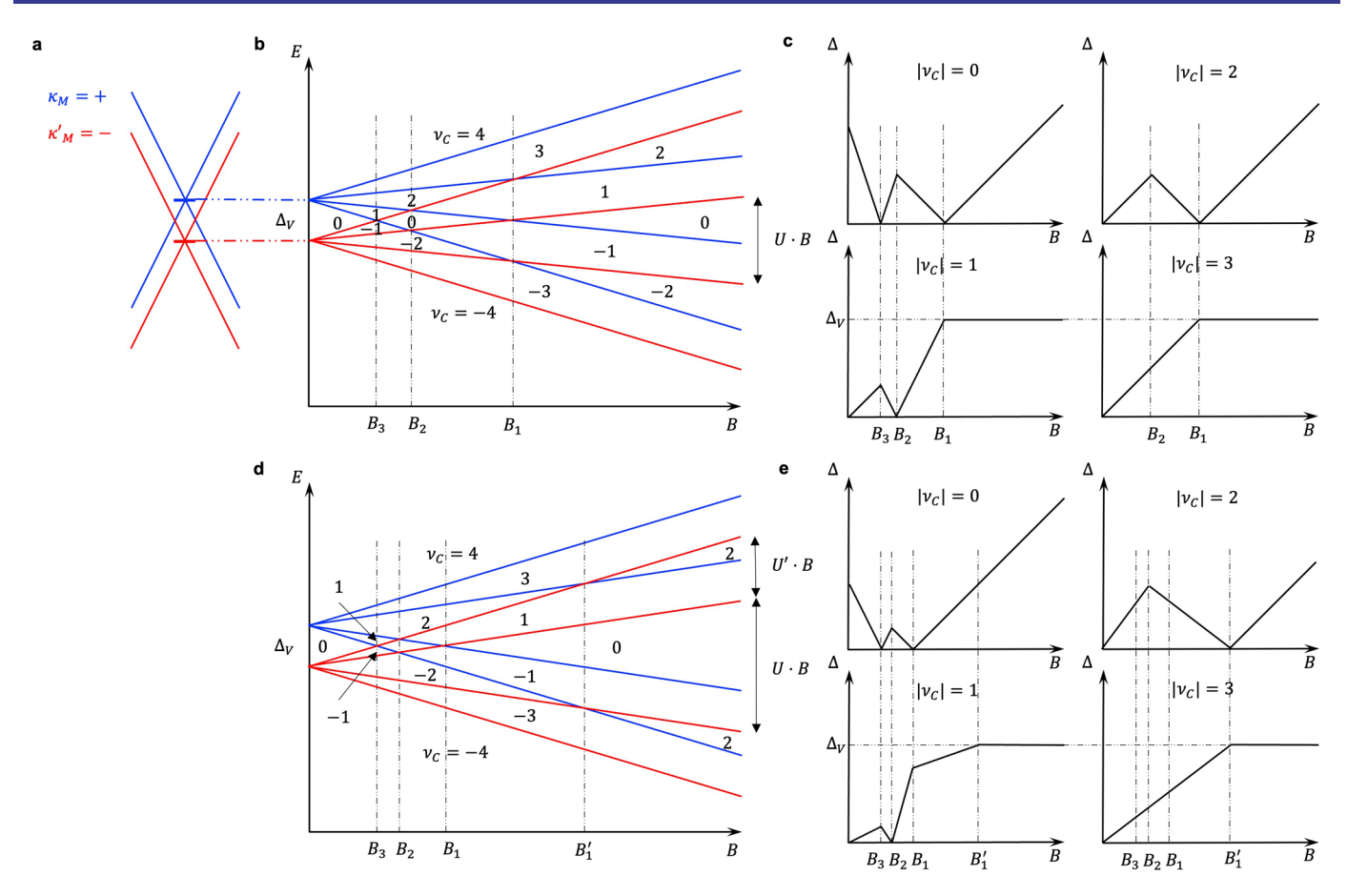
Extended Data Fig. 7 | Hofstadter spectrum from a second location. Correlated Hofstadter spectrum extracted from the data in Extended Data Fig. 4. The spectrum qualitatively agrees with that in Fig. 2c with a slightly smaller total bandwidth.



Extended Data Fig. 8 | Hysteresis as a function of B. $d\mu/dn$ measured as a function of both increasing (red) and decreasing (blue) B at fixed densities. Hysteretic regions are highlighted in yellow. **d-e**, Hysteresis as a function of density, reproduced from Fig. 3a, d. Overlaid yellow lines indicate ranges over which we observe hysteresis as a function of B. Solid (dashed) lines indicate $d\mu/dn_{up} - d\mu/dn_{down} > 0$ (<0), respectively. The ranges of ν and B in which hysteresis occurs are independent of which is swept as the fast axis.



Extended Data Fig. 9 | zLL gap evolution at a second location. Thermodynamic gaps of $\nu_C = \pm 2$ zLLs extracted from the data presented in Extended Data Fig. 4.



Extended Data Fig. 10 | Phenomenological model of zLL evolution in the presence of mirror symmetry breaking. Schematic of the moiré valley splitting Δ_v between κ_M , κ_M' by Δ_v . **b**, Evolution of the zLLs in the presence of inter-flavor Coulomb repulsion U (ignoring single-particle effects). Four zLLs with different flavors are split linearly in B within each moiré valley (red and blue, respectively), resulting in LL crossings. The corresponding Chern numbers are labeled within the gaps. **c**, B dependence of zLL gaps derived from **b**. **d**, Evolution of the zLLs if the Zeeman coupling is different for spin and valley flavors. Such single-particle gaps lead to different effective interactions U and U' between LLs corresponding to different flavors within each moiré valley. This modifies the fields at which LL crossings occur, reducing B_1 , B_2 and B_3 relative to the predicted field B_1' at which the gaps at $|\nu_c| = 2$ close and those at odd integer fillings saturate. **e**, B dependence of the zLL gaps derived from **d**.